JOURNAL OF GEOPHYSICAL RESEARCH, VOL. 101, NO. D1, PAGES 1621–1634, JANUARY 20, 1996

Observational evidence of plane parallel model biases: Apparent dependence of cloud optical depth on solar zenith angle

Norman G. Loeb and Roger Davies[1]

Department of Atmospheric and Oceanic Sciences, McGill University, Montreal, Québec, Canada

Abstract. This study directly compares plane parallel model calculations with 1 year of Earth Radiation Budget Satellite shortwave observations at nadir over ocean between 30°S and 30°N. When plane parallel model calculations are matched to the observations on a pixel-by-pixel basis by adjusting cloud fraction and cloud optical depth, the resulting frequency distributions of cloud optical depth show a systematic shift towards larger values with increasing solar zenith angle, regardless of the assumptions made in the calculations. This dependence is weak for thin clouds but gets progressively stronger as the clouds become thicker. For the thinnest 50% of the clouds (optical depths $\lesssim 6$), it occurs only at oblique solar zenith angles, whereas it is observed at all solar zenith angles for the thickest 10% of clouds (optical depths $\gtrsim 12$). On average, the increase is extremely large for solar zenith angles $\gtrsim 63°$. Such behavior is unrealistic since average cloud optical depths from such an extensive data set should be almost independent of solar zenith angle. The cause is traced to a fundamental flaw in plane parallel theory applied to real clouds: the solar zenith angle dependence of model reflectance is opposite to that of the observations. The one-dimensional nadir reflectance remains within 10% of the observed reflectance for solar zenith angles $\lesssim 53°$ when applied to a general ensemble of real clouds, and for solar zenith angles $\lesssim 63°$ when applied to the thinnest 50% of such clouds. Uncertainties are found to increase rapidly as the Sun becomes more oblique, easily reaching 30% at the lowest solar elevations. Based on results from theoretical studies, it is concluded that three-dimensional cloud structures not accounted for by plane parallel theory have a statistically important effect on the radiation field. As a minimum requirement, application of one-dimensional theory to the remote sensing of cloud optical thickness from measurements of nadir reflectance should therefore be restricted to thin clouds and small solar zenith angles.

1. Introduction

The remote sensing of cloud optical thickness from satellite-measured radiances, in addition to many other applications, conventionally adopts the plane parallel assumption which considers clouds to be (locally) one dimensional and therefore horizontally invariant. We know from experience, however, that real clouds occur with a wide variety of shapes and sizes that have obvious three-dimensional characteristics, and one might reasonably expect there to be many discrepancies between one- and three-dimensional approaches. Here we address only one aspect of the dichotomy between three-dimensional reality and one-dimensional remote sensing of cloud optical properties, namely, the effect of solar zenith angle on the cloud optical depths inferred from shortwave radiance observations.

Ample theoretical evidence [e.g., *Busygin et al.*, 1973; *McKee and Cox*, 1974; *Aida*, 1977; *Davies*, 1978, 1984; *Bréon*, 1992; *Kobayashi*, 1993] has already shown that reflectivities from specific types of three-dimensional clouds can differ substantially from those assumed to be plane parallel. There is also increasing observational evidence [e.g., *Stuhlmann et al.*, 1985; *Coakley and Davies*, 1986; *Minnis*, 1989; *Coakley*, 1991] consistent with such theory. These studies clearly demonstrate that three-dimensional effects are important for certain types of clouds, so that one-dimensional retrieval of cloud optical depth may be substantially biased. Additional observational studies are now needed to quantify this bias for mixtures of cloud types that are representative of general conditions.

[1]Now at Institute of Atmospheric Physics, University of Arizona, Tucson.

Paper number 95JD03298.
0148-0227/96/95JD-03298$05.00

In a recent study of nonspecific cloud type effects, *Davies* [1994] analyzed the angular dependence of spatial autocorrelation functions of broadband shortwave and longwave Earth Radiation Budget Satellite (ERBS) scanner measurements. He showed that general cloud scenes violate the principle of directional reciprocity, which is a necessary condition for such scenes to be treated as horizontally homogeneous. He did not, however, directly assess the error in treating them as homogeneous.

The present study extends the work of *Davies* [1994] by examining the limitations of the plane parallel assumption when applied to retrieve cloud optical depths for near-nadir views at different solar elevations, a common remote sensing problem. The analysis relies on the statistical information content of a very large number of observations, stratified by solar zenith angle. As discussed below, the data set is restricted to oceanic scenes equatorward of 30° and to viewing angle cosines between 0.9 and 1. These restrictions avoid complications due to sampling biases, changes in underlying surface albedo, strong diurnal effects, and expansion effects of the viewed area at larger off-nadir angles. The analyzed data are sufficiently nonrestrictive, however, that they encompass a wide range of general cloud types. Cumuliform clouds, for which three-dimensional effects are likely to be strong, are well represented in this latitude range. A range of stratiform clouds are also represented, but not as frequently as at higher latitudes. Cloud types unique to continental and high-latitude conditions are missing from this study.

In the following we describe the data used and the development of a reasonably sophisticated one-dimensional analysis procedure in more detail, as well as the results obtained. The absence of measured data to constrain the input variables to the analysis, especially the lack of information on the subpixel cloud fraction which completely handicaps the analysis of a single scene, is shown to be much less of a problem when the data are analyzed statistically. Consistent results are in fact obtainable for a wide range of input assumptions. Biases in the optical depths retrieved one dimensionally are shown to depend on solar zenith angle, particularly so at large solar zenith angles. These biases could, loosely put, be attributed to various combinations of (1) nonlinear averaging of subpixel inhomogeneity, (2) the effect of cloud sides, affecting illuminated and viewed cloud cross sections, as well as allowing loss of radiation, (3) cloud top structure, and (4) internal cloud inhomogeneity. The relative influence of these effects is briefly considered, but not analyzed in depth.

2. Observed Reflectances

Observed reflectances are determined from ERBS scanner shortwave radiance measurements as follows:

$$R(\mu, \mu_0, \phi) = \frac{\pi I(\mu, \mu_0, \phi)}{\mu_0 F} \times 100\% \qquad (1)$$

where

- I shortwave pixel radiance;
- F solar constant (=1365 W m^{-2}) corrected for the Earth-Sun distance;
- μ cosine of the observer zenith angle;
- μ_0 cosine of the solar zenith angle;
- ϕ azimuth angle relative to the solar plane ($\phi = 0°$ corresponds to forward scattering).

The scanner instrument aboard the ERBS satellite measures radiance in three broadband intervals: shortwave (0.2 to 5 μm), longwave (5 to 50 μm) and total (0.2 to 50 μm) [*Kopia*, 1986; *Barkstrom et al.*, 1989]. The scan is perpendicular to the orbital track with a field of view of about 31×47 km^2 at nadir, increasing to about 550×150 km^2 at the limb. The ERBS orbit is in a 57° inclination which precesses 4.95° west per day, allowing measurements from many different Sun-Earth-satellite viewing configurations to be sampled during the course of 1 month.

One year (from November 1984 to October 1985) of near-nadir pixel-level (S-8) measurements for μ between 0.9 and 1.0 are considered here. Only scenes over ocean between 30°S and 30°N are included in order to avoid complications arising from strong diurnal effects and surface inhomogeneities, and because albedos over ocean are generally quite small compared to those from clouds (outside of the sunglint region). Tropical latitudes were selected because there tends to be a higher frequency of occurrence of cumuliform clouds than at higher latitudes [*Warren et al.*, 1988]. As a result, the tropics provide a good testbed for examining how the plane parallel model compares with observations.

3. Plane Parallel Calculations

Since the ERBS scanner footprint can exceed the size of individual cloud elements, many of the measurements from ERBS are taken from mixed scenes, that is, scenes composed of both clear and subpixel cloud regions. The sensitivity to such inhomogeneities in the plane parallel calculations can be evaluated by neglecting three-dimensional effects and assuming the radiance is a linear function of cloud fraction (f). Thus reflectances from pixels which are partly filled by a single-layer cloud can be approximated as

$$R = (1 - f)R^{CLR} + fR^{CLD} \qquad (2)$$

where R^{CLD} is the shortwave reflectance contribution from the cloudy portion of the pixel (depends on cloud optical depth τ_p) and R^{CLR} is the shortwave reflectance contribution from the clear sky portion of the pixel.

Alternately, another commonly used approach in satellite remote sensing is to assume the pixels are homogeneous, either overcast or clear. This removes 1 degree of freedom in the calculations since cloud fraction is always unity for cloudy pixels. This approach has merit provided that the spatial resolution of the measurements is sufficiently high. While this is not the

case in this study (due to the low resolution of ERBS measurements), this approach is nonetheless considered here along with the inhomogeneous approximation, for comparison purposes. The following sections describe how the R^{CLD} and R^{CLR} values are obtained.

3.1. Cloud Reflectance Calculations

Modeling the transfer of radiation from cloudy atmospheres across broad spectral intervals requires that the spectral variation of both cloud and clear sky scattering and transmission be taken into account. Look-up tables of R^{CLD} as a function of viewing geometry and cloud optical depth were generated using the DISORT program of *Stamnes et al.* [1988] which is based on the discrete ordinates method. Forty-eight streams were used in all calculations, and Earth curvature effects were also accounted for. The atmosphere was divided into four homogeneous vertical layers corresponding to a lower boundary layer, a cloud layer, a tropospheric layer, and a stratospheric layer. Reflection from the ocean surface below the cloud layer was obtained using the Lambertian model with an albedo of 7%. A cloud-top height of 3 km was used in the calculations based on International Satellite Cloud Climatology Project results [*Rossow and Schiffer*, 1991] from 1 year of satellite observations over ocean which found the average cloud-top height occurred at the 3-km level. In order to examine the uncertainty due to this assumption, calculations were also carried out for a cloud-top height of 6 km, and for the case where no atmosphere was present above or below the cloud.

Scattering in the layers above and below the cloud layer consisted of both molecular and aerosol scattering. All clear sky optical depths, aerosol phase functions, and single scattering albedos for the boundary layer, troposphere, and stratosphere were obtained directly from the LOWTRAN-7 model [*Kneizys et al.*, 1988]. Figure 1 shows the 0.5-μm clear sky optical depth profiles used for ozone absorption, aerosol scattering, molecular scattering, and the total. Since aerosol concentrations can show rather large temporal and spatial variations over ocean [*Prospero et al.*, 1983; *Hoppel et al.*, 1990], the largest uncertainty in these profiles is associated with the aerosol component. In this study an aerosol optical depth of 0.1 at the surface was assumed based on the studies of *Toon and Pollack* [1976] and *Durkee et al.* [1991] who found aerosol optical depths typically ranged between 0.05 and 0.2 over ocean.

Within the cloud layer, drop-size distributions were given by Deirmendjian's C.1 cloud model [*Deirmendjian*, 1969]. Single scattering properties were calculated using the Mie scattering code of *Bohren and Huffman* [1983] using refractive indices from *Hale and Querry* [1973]. Only one cloud microphysical model is considered because broadband shortwave reflectances for a given optical depth tend to be insensitive to the cloud microphysics. As an example, when reflectances generated using the C.1 model (effective radius 6 μm) were compared with those generated using a modified gamma size distribution having an effective droplet radius of 10 μm, relative reflectance differences tended to be quite small (< 5%), and no systematic dependence on μ_0 was observed in the differences. Also, no account of absorption by water vapor within the cloud was included since absorption is largely dominated by water droplets when water vapor absorption above the cloud is taken into account [*Davies et al.*, 1984].

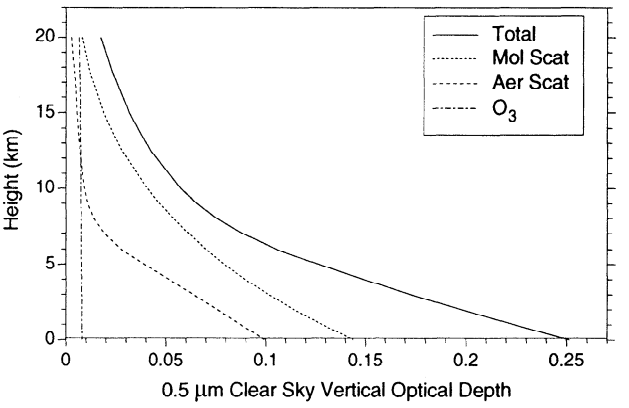

Figure 1. The 0.5-μm clear sky vertical optical depth profiles of ozone, aerosol scattering, molecular scattering, and the total.

The look-up tables consist of R^{CLD} determined for 24 optical depths (defined at 0.55 μm) between 0.5 and 200, view and solar zenith angles between 0°and 89°, and 19 azimuth angles between 0° and 180°. In order to avoid excessive computational times in generating the look-up tables, the spectral resolution was set no higher than necessary. Radiance calculations involving the cumulus cloud model in LOWTRAN-7 were compared for two different wavenumber resolutions ($\Delta\nu$): (1) $\Delta\nu = 50$ cm^{-1} over the complete shortwave interval 2000 to 50,000 cm^{-1} and (2) $\Delta\nu = 1000$ cm^{-1} for wavenumbers between 4000 and 34,000 cm^{-1}. While the coarser resolution of $\Delta\nu = 1000$ cm^{-1} did not represent fine-scale features in the radiance dependence on wavenumber very well, agreement in the integrated or broadband radiance between the two different resolutions was very good. Overall, relative differences were less than 3%, regardless of Sun-Earth-satellite geometry. Therefore look-up tables were generated using the lower resolution of $\Delta\nu = 1000$ cm^{-1} over the 4000 to 34,000 cm^{-1} range.

3.2. Clear Sky Reflectances

Rather than rely on model calculations of clear sky reflectance (R^{CLR}), the approach used here was to derive representative clear sky reflectances directly from 1 year of observations. The first step was to define an initial nadir clear sky longwave threshold in order to identify the pixels having the greatest probability of actually being cloud-free. Considering only pixels flagged as clear by the Earth Radiation Budget

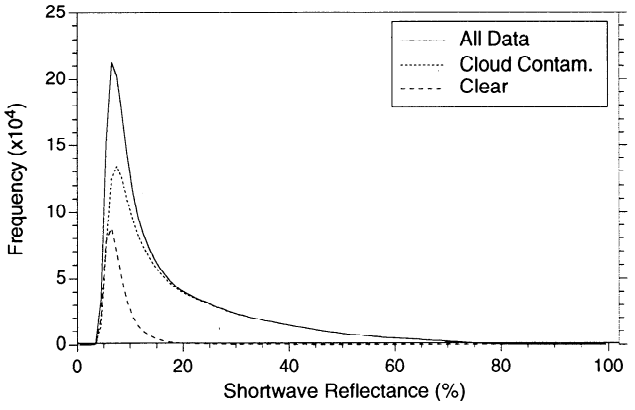

Figure 2. Observed shortwave reflectance frequency distribution for $\mu = 0.9$–1.0 and $\mu_0 = 0.5$–0.6 for all data ("All Data"), only data remaining after the longwave cutoff is applied ("Cloud Contam."), and for pixels identified as clear ("Clear").

Experiment (ERBE) maximum likelihood estimation (MLE) technique [*Wielicki and Green*, 1989], an initial clear sky longwave threshold corresponding to the peak in the relative frequency distribution for these pixels was defined. Next, by analyzing shortwave reflectance frequency distributions of only those pixels that were warmer than this clear sky longwave cutoff, representative clear sky reflectances for each μ_0 bin were derived in a similar manner. As an example, Figure 2 shows one such shortwave reflectance frequency distribution (labeled "clear") for $\mu_0 = 0.5-0.6$. Also shown for comparison are frequency distributions of all pixels in this μ_0 range ("all data"), and of pixels having a longwave radiance lower than the longwave cutoff ("cloud contam."). From the "clear" frequency distribution, a representative clear sky reflectance was defined for each μ_0 bin by the reflectance corresponding to the peak of the distribution (for μ_0= 0.5–0.6, this corresponds to a shortwave reflectance of 6.5%).

4. Analysis Approach

4.1. Sampling Considerations

To avoid introducing uncertainties due to factors not accounted for in the plane parallel calculations, clear scenes and scenes consisting of thick overcast ice clouds were excluded from the analysis. The latter scene types were not included since no provision for scattering by ice crystals was made in this study. The ERBE clear scene identifier was used to exclude clear scenes (this is likely to be a conservative choice since the ERBE "clear" category may contain ≈5% cloud cover). Scenes consisting of thick overcast ice clouds were more difficult to identify, however. Based on LOWTRAN-7 model calculations [*Kneizys et al.*, 1988] and results from previously published observational studies, longwave thresholds were defined that exclude the coldest scenes. LOWTRAN-7 calculations involving thick cirrus clouds under tropical atmospheric conditions were performed for cloud top heights ranging from 8 to 11 km. Table 1 shows broadband and 11-μm brightness temperatures obtained for these cases. Broadband brightness temperatures ranged from 230 K (for cloud tops at 11 km) to 245 K (for tops at 8 km), while the corresponding 11-μm brightness temperatures ranged from 233 to 256 K. *Machado et al.* [1992] explored a range of 11-μm brightness temperatures based on Meteosat satellite measurements and found 11-μm brightness temperatures ranged from 207 to 253 K (for cloud top heights between 14.5 and 8 km). Based on these results, a conservative broadband longwave threshold of 245 K (corresponding to an 11-μm brightness temperature of 256 K) was selected to exclude thick ice clouds from the analysis. Since the objective here is to consider water clouds only, this choice of threshold appears to be reasonable. Based on an analysis of ERBS nadir observations, this threshold was found to remove the coldest 10% of all pixels and to cause average shortwave reflectances to decrease by approximately 3%. It should be noted that, while this technique will filter out very cold, thick, overcast ice clouds, it will not necessarily exclude all thin or subpixel ice clouds since longwave radiances in such cases can be quite similar to those from scenes containing only water clouds. The effect of inadvertently retaining some thin or partly cloudy ice cloud scenes in the analysis is expected to have a minor effect on the average shortwave reflectance dependence on μ_0 since, as will be shown in section 5, the same dependence on μ_0 is observed even when thick ice clouds are included.

Table 1. Broadband and 11-μm Brightness Temperatures From LOWTRAN 7 Runs Involving Thick Cirrus Clouds as a Function of Cloud-Top Height

Cirrus Cloud-Top Height, km	Broadband Brightness Temperature, K	11-μm Brightness Temperature, K
8	245.1	256.5
9	240.4	250.1
10	235.4	243.8
11	230.0	233.4

4.2. Model Fits to Observations

In order to examine the consistency between the plane parallel model and observations, cloud optical depths and cloud fractions are first inferred on a pixel-by-pixel basis to ensure a match between the calculations and observations. Once this is done for 1 year of observations, the resulting distributions of cloud optical depth are then examined. Provided diurnal and latitudinal biases in the observations are small, and provided cloud optical depths and cloud fractions are derived in a consistent manner for all μ_0, one would expect both of these parameters to remain constant with μ_0 since there are no other physical grounds for them to vary. Therefore any systematic departure from this behavior would most likely be due to limitations in the plane parallel model approach.

Given the rather large field of view associated with ERBS scanner data, cloud fractions and cloud optical depths can be inferred only in a very approximate manner. Thus the aim here is not to produce "climatologies" of cloud fraction and cloud optical depth but rather to show that the conclusions drawn about the dependence of τ_p on μ_0 are not sensitive to how cloud fraction is determined.

Initial estimates of cloud fraction (f) are obtained from observed longwave and shortwave radiances from the following:

$$f_{LW} = \frac{(I_{LW}^{PIX} - I_{LW}^{CLR})}{(I_{LW}^{CLD} - I_{LW}^{CLR})} \quad (3)$$

$$f_{SW} = \frac{(I_{SW}^{PIX} - I_{SW}^{CLR})}{(I_{SW}^{CLD} - I_{SW}^{CLR})} \quad (4)$$

where I_{SW}^{PIX} and I_{LW}^{PIX} are observed shortwave and longwave pixel radiances, respectively, and I_{SW}^{CLR}, I_{LW}^{CLR}, I_{SW}^{CLD}, and I_{LW}^{CLD} are representative shortwave and longwave clear and overcast radiances. I_{SW}^{CLD} and I_{LW}^{CLD} were subjectively determined so as to ensure a constant average cloud fraction of 0.4 at all solar zenith angles (based on cloud fractions derived from the ERBE MLE technique), while I_{SW}^{CLR} and I_{LW}^{CLR} were defined by the clear sky threshold values described earlier. In general, f_{SW} and f_{LW} will not be identical. Since shortwave radiances from cloudy scenes are affected by more degrees of freedom than are longwave radiances, more uncertainty in the shortwave estimate of cloud fraction is expected. However, if cloud top temperatures are very similar to the sea surface temperature, f_{LW} will tend to underestimate the cloud fraction, so that f_{SW} would likely be more representative. Therefore an effective cloud fraction which uses both f_{LW} and f_{SW} is desirable since both of these values provide valuable information on cloud cover. Thus estimates of cloud fraction (f) are obtained by simply averaging f_{LW} and f_{SW}.

Once a value of cloud fraction has been obtained, the next step is to determine a cloud optical depth which ensures a match between the plane parallel reflectance and the pixel observation. Letting the observed shortwave reflectance equal R in (2), and using R^{CLR} to represent the clear sky reflectance, the corresponding reflectance from the cloudy portion of the pixel (R^{CLD}) is obtained. Next, this value is inverted using the plane parallel cloud model, and a 0.55-μm τ_p is inferred from the reflectance-cloud optical depth look-up tables described in section 3.1.

Figures 3a and 3b show contour plots of shortwave reflectance as a function of cloud optical depth and cloud fraction. As shown, many different cloud optical depth/cloud fraction combinations produce the same reflectance. Further, the sensitivity of the reflectance on these parameters appears to be more pronounced at $\mu_0 = 0.55$ than at $\mu_0 = 0.15$. In order to account for the wide range of possible cloud fraction/τ_p combinations in the comparisons, both the inhomogeneous pixel approximation and the homogeneous pixel approximation are used. These two approaches are quite different in

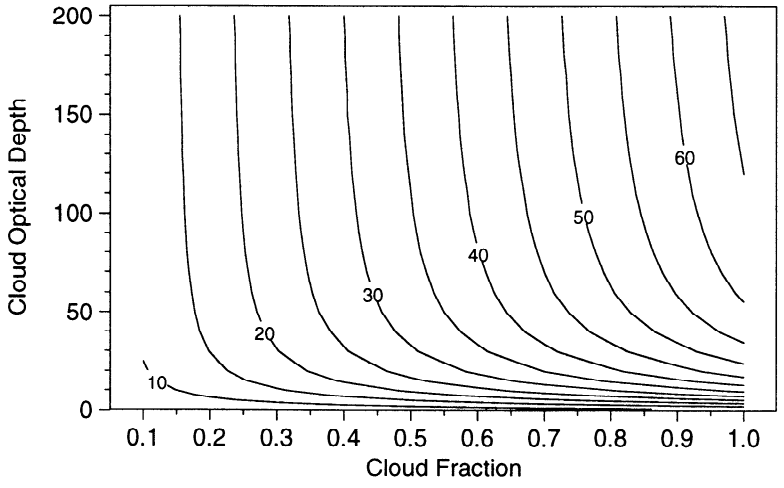

Figure 3a. Contours of calculated shortwave reflectance at nadir as a function of cloud optical depth and cloud fraction for $\mu_0 = 0.55$ for a cloud-top height of 3 km.

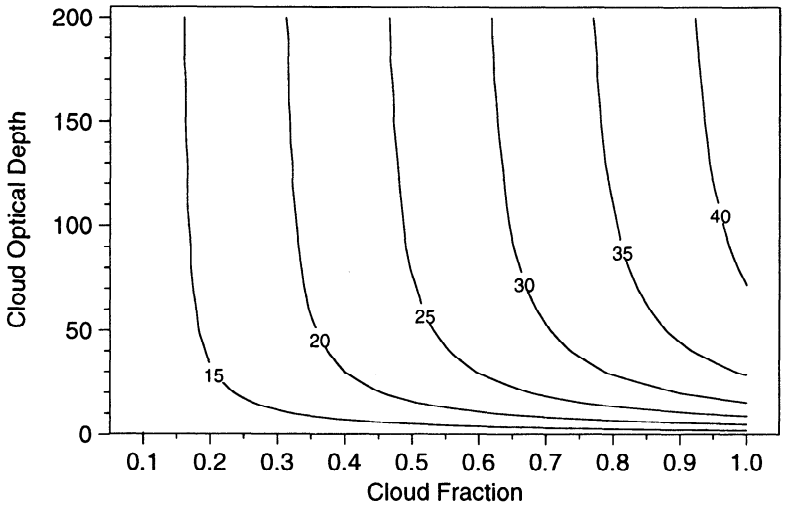

Figure 3b. Contours of calculated shortwave reflectance at nadir as a function of cloud optical depth and cloud fraction for $\mu_0 = 0.15$ for a cloud-top height of 3 km.

practice. In the inhomogeneous pixel approximation, f varies from pixel to pixel along with cloud optical depth (τ_{nh}), while in the homogeneous pixel approximation, cloud fractions are fixed at unity and the cloud optical depth (τ_h) consequently tends to be much lower than τ_{nh}. Finally, in order to account for uncertainties due to clear sky effects above/below the cloud layer, comparisons between observations and calculations are performed using cloud top heights of 3 and 6 km, and for the case where clear sky effects are ignored.

4.3. Error Analysis

Uncertainties in mean reflectance due to sampling errors are calculated from the standard error in the mean, taking into account the high degree of spatial correlation between pixels, which gives rise to a correlation radius of ≈500 km. Based on *Davies* [1994], the error in the mean reflectance can be obtained from

$$E = \pm \frac{\sigma}{\sqrt{N}} \left\{ 1 + 2 \sum_{r=1}^{N-1} \left(1 - \frac{r}{N}\right) \rho(r) \right\}^{1/2} \quad (5)$$

where σ is the standard deviation for N observations, and $\rho(r)$ is the autocorrelation at lag r given by

$$\rho(r) = \frac{\mathrm{cov}(\mathrm{I_i}, \mathrm{I_{i+r}})}{\sigma(I_i)\sigma(I_{i+r})} \quad (6)$$

and $\mathrm{cov}(I_i, I_{i+r})$ is the covariance in radiance for fields of view along the satellite track r pixels apart.

Because of the very large number of observations used in this study (N > 500,000), errors in mean reflectance tend to be quite small, generally less than 0.15% in absolute reflectance. Consequently, in most of the graphs of mean reflectance shown in section 5, error bars have not been included. Uncertainties in reflectance frequency distributions were also small, at less than 1%.

Estimates of cloud optical depth for any given scene will tend to suffer from rather large uncertainties given the complexity of cloud scenes at scales as large as the ERBS pixel. The largest uncertainty will lie in the estimate of cloud fraction: simple threshold techniques become less reliable in general as pixel resolution decreases [*Wielicki and Parker*, 1992]. Other sources of uncertainty include the effect of attenuation above the cloud top by the atmosphere, uncertainties in cloud microphysics, uncertainties due to the use of a lower spectral resolution, and uncertainties due to the Lambertian model used to calculate reflection contributions from the ocean surface below the cloud layer. For the purpose of this study, however, the most important errors are those which show a systematic dependence on μ_0. Such model bias errors would tend to obscure any systematic differences between the observations and calculations with μ_0 which may be attributable to inherent limitations of the plane parallel model assumption. In the following section, we demonstrate that regardless of how the plane parallel calculations are carried out, bias errors due to the plane parallel model assumption tend to dominate.

5. Results

Before making direct comparisons between the observations and plane parallel calculations, it is useful to first examine the observations alone. Figure 4 shows average observed reflectances versus μ_0 for all pixels throughout the year ("All Obs"), for pixels which were not rejected as being clear or containing thick ice clouds ("Obs Analyzed"), and when clear pixels were not included ("No Clr"). In all cases, the reflectance appears to increase with decreasing μ_0. Reflectances for the "Obs Analyzed" case are lower than the other two cases because excluding thick ice clouds tends to lower the average reflectance. Since the relative dependence of the

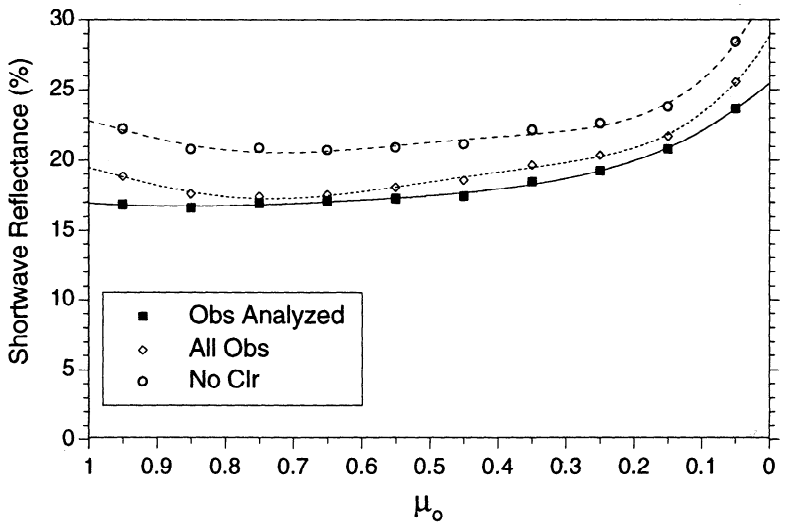

Figure 4. One-year average observed shortwave reflectances versus μ_0 for pixels which were not rejected as being either clear or containing thick ice clouds ("Obs Analyzed"), and for all observations throughout the year ("All Obs").

observed shortwave reflectance on μ_0 shows very little change regardless of whether or not thick ice clouds are included, it is unlikely that the presence of undetected thin or partly cloudy ice clouds will influence this dependence either. The tendency for reflectances to increase as μ_0 decreases is also very apparent in the reflectance frequency distributions. This is illustrated in Figure 5 which shows reflectance frequency distributions for various μ_0 values (for the "Obs Analyzed" case). At large μ_0, the frequency distributions are rather similar for $\mu_0 > 0.5$, but as μ_0 decreases, the peak in the distributions tends to occur at progressively higher reflectance values, and the distributions begin to broaden rather dramatically.

In order to test whether or not this behavior in the observed reflectance is attributable to diurnal effects, the observations were stratified according to whether they occurred in the morning or afternoon, local time. This comparison, shown in Figure 6, reveals that while the morning and afternoon reflectances are statistically different for high to moderate solar elevations, they are in close agreement at low elevations, and both morning and afternoon reflectances show a similar systematic increase with decreasing μ_0. The fact that morning observations appear to be slightly larger than afternoon values is consistent with results from other satellite-based studies on the diurnal behavior of cloud properties over ocean [*Minnis and Harrison*, 1984; *Hartmann and Recker*, 1986]. Overall, these studies have found a maximum in low-level cloudiness and a minimum in cloud-top temperature during the morning, and a minimum in cloudiness and a maximum in cloud-top temperature during the late afternoon. They note, however, that diurnal effects over ocean are much less pronounced

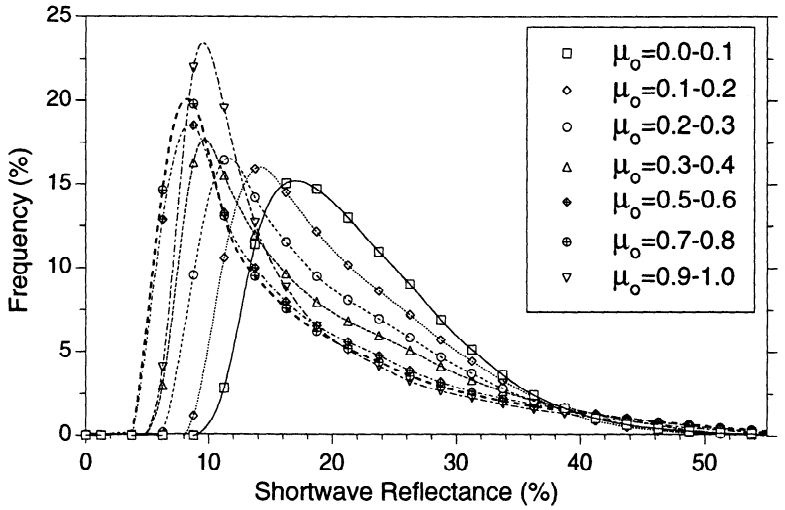

Figure 5. Observed shortwave reflectance frequency distributions at $\mu = 0.9$–1.0 for various μ_0 bins for observations not rejected as being either clear or containing thick ice clouds.

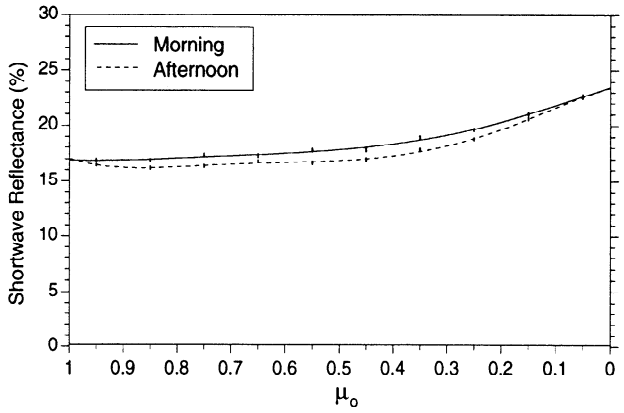

Figure 6. One-year average observed shortwave reflectances versus μ_0 for pixels which were not rejected as being either clear or containing thick ice clouds stratified by morning and afternoon local time.

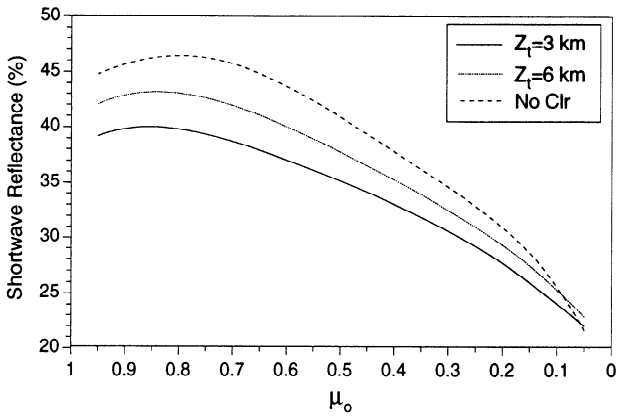

Figure 8. Broadband shortwave reflectance calculations versus μ_0 for a cloud with optical depth 10, cloud fraction 1, and cloud top heights of 3 and 6 km, as well as for the case where clear sky effects above and below the cloud are not included in the calculation.

than those over land. Thus, while weak diurnal effects are indeed present in the oceanic observations, they are not the main reason for the increase in reflectance with decreasing μ_0 found in the mean reflectance.

In order to examine whether latitudinal biases are present in the observations, observations were also stratified according to whether they fall in the 0°−15° or 15°−30° latitude ranges. This is illustrated in Figure 7 which shows the fraction (in percent) of pixels lying in both these latitude bins. For $\mu_0 < 0.6$, the proportion of pixels from both these latitude ranges is reasonably constant. Approximately 55% of the pixels fall in the 15°−30° latitude range, while about 45% lie between 0° and 15°. Not surprisingly, when the Sun is closer to zenith, a much larger fraction of pixels occurs in the 0°−15° latitude range. Despite this oversampling, there does not appear to be any significant effect on the observed reflectance frequency distributions in Figure 5; at $\mu_0 = 0.9 - 1.0$, the reflectance frequency distribution appears to be quite similar to those at intermediate μ_0 (where the fraction of samples in the 0°−15° latitude range is much lower). The marked differences in the reflectance frequency distributions for $\mu_0 < 0.6$ cannot

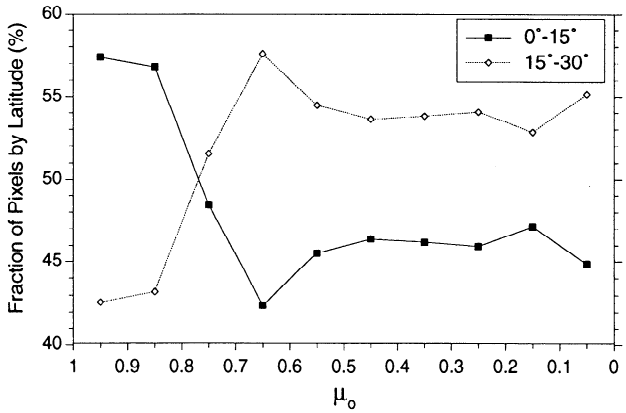

Figure 7. Fraction of nadir observations falling between the 0°–15° and 15°–30° latitude zones.

therefore be attributed to latitudinal effects since the latitudinal sampling appears nearly constant there.

Since neither diurnal nor latitudinal effects have a significant influence on the observed frequency distributions, we conclude that the intrinsic cloud properties of this data set do not depend on μ_0. Further, for the plane parallel assumption to be applicable, we would expect the model reflectance dependence on μ_0 for constant τ_p to agree with observations. When constant cloud fraction and cloud optical depth values are used in plane parallel model calculations for different μ_0, an interesting result occurs. Figure 8 shows plane parallel model reflectance calculations at nadir for a cloud optical depth of 10 and a cloud fraction of 1.0 for three different conditions: (1) a cloud top of 3 km; (2) a cloud-top height of 6 km; and (3) when clear sky effects above and below the cloud are not included in the calculation. The lower altitude clouds have smaller reflectances because of increased attenuation by the atmosphere above the cloud top. In each case, calculated reflectances decrease with decreasing μ_0. This result is in stark contrast to the observations. The tendency for the plane parallel calculations to decrease with decreasing μ_0 appears to become more pronounced for thicker clouds. Figure 9 shows plane parallel reflectance calculations as a function of τ_p for $\mu_0 = 0.15$ and $\mu_0 = 0.5$ for the same cloud models as in Figure 8. For small τ_p very little dependence on μ_0 is observed, but as the cloud gets thicker the reflectance decreases strongly as $\mu_0 \to 0$.

At small τ_p, slight errors in the calculations are expected due to uncertainties associated with the use of the Lambertian model in calculating reflection contributions from the ocean surface below the cloud layer. The largest uncertainties would likely occur at Sun-Earth-satellite geometries where Sun glint from the ocean surface is a maximum. At nadir, this effect would tend to be most pronounced for overhead Sun, and would

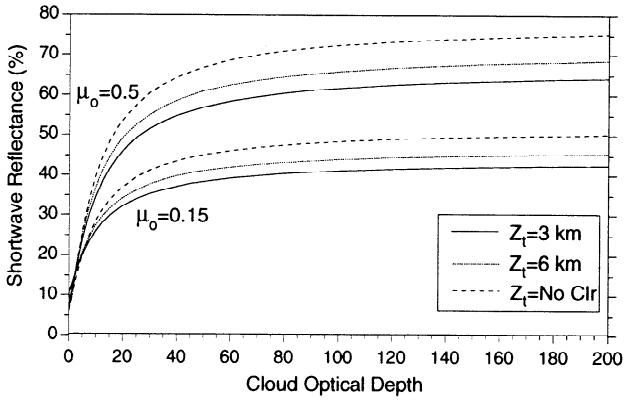

Figure 9. Broadband shortwave reflectance calculations versus cloud optical depth for $\mu_0 = 0.5$ (top three curves) and $\mu_0 = 0.15$ (bottom three curves) for cloud top heights of 3 and 6 km, as well as for the case where clear sky effects above and below the cloud are not included in the calculation.

be negligible at small μ_0 [*Koepke and Quenzel*, 1979]. Thus, while inclusion of Sun glint in the calculations might cause a slight increase in reflectance at overhead Sun, it would not alter the tendency for the reflectance to decrease with decreasing μ_0, as shown in Figure 8.

When the plane-parallel calculations are matched to the near-nadir observations using the inhomogeneous and homogeneous pixel approximations, the resulting values of τ_p show a strong dependence on μ_0. For the inhomogeneous pixel case, cloud fractions were derived from thresholds which were preselected so as to ensure a constant yearly mean cloud fraction of 0.4, while for the homogeneous case, a constant cloud fraction of 1.0 was assumed for all cloudy pixels. Figure 10 shows 1-year average values of τ_p as a function of μ_0 (for a representative cloud-top altitude of 3 km). For the inhomogeneous approximation, τ_{nh} depends most strongly on μ_0 for $\mu_0 < 0.45$. Between $\mu_0 \approx 0.95$ and $\mu_0 \approx 0.55$, τ_{nh} increases gradually from ≈ 6 to ≈ 9, and then increases rapidly to ≈ 100 at $\mu_0 \approx 0.05$. By comparison, the μ_0 dependence in cloud optical depth is less pronounced for the homogeneous pixel approximation. Between $\mu_0 \approx 0.95$ and $\mu_0 \approx 0.25$, τ_h increases from ≈ 3 to ≈ 5, and reaches ≈ 18 for $\mu_0 \approx 0.05$. Note that cloud optical depths are likely underestimated by at least a factor of 2 for this case since subpixel cloud fractions are not accounted for.

The larger increase in τ_{nh} for the inhomogeneous case is expected since, as shown in Figure 9, calculated reflectances tend to show a much greater sensitivity to μ_0 when τ_p is larger. To demonstrate the dependence of average τ_p on μ_0 more systematically, the τ_p values were divided into different classes of occurrence of cloud optical depth. Figure 11 shows analogous results to Figure 10, but for each class of occurrence. Here the 0–50% line represents the average τ_p for cloud optical depths lying below the 50th percentile (i.e., over the smallest half of each cloud optical depth distribution), the 50–75% line represents the average τ_p for optical depths lying between the 50th and 75th percentiles, etc. The increases in both τ_h and τ_{nh} with decreasing μ_0 tend to be small for the lower classes of τ_p (optical depths $\lesssim 6$), while they are much more pronounced for the largest classes. In fact, the rise in τ_p with decreasing μ_0 is extremely large at all solar zenith angles for classes with $\tau_p \gtrsim 12$ at $\mu_0 \approx 0.95$. For these cases, cloud optical depths more than double between $\mu_0 = 0.95$ and $\mu_0 = 0.45$. This occurs for the inhomogeneous pixel approximation for the (optically) thickest 10% of the clouds, and in the homogeneous pixel approximation for the (optically) thickest 1% (99–100% class).

Figures 12a and 12b show cloud fraction and τ_p frequency distributions resulting from the comparison of the inhomogeneous pixel approximation with the observations. In Figure 12a, only pixels identified as cloud contaminated were included in the cloud fraction frequency distribution. While thresholds were preselected to provide an overall average cloud fraction of 0.4 at all μ_0 (based on ERBE MLE cloud fractions), no other constraints on the relative frequency distribution were imposed. As shown, the cloud fraction distributions appear quite similar for all μ_0. This is expected since, on average, cloud fraction should be independent of μ_0 in the absence of strong latitudinal and diurnal effects. In contrast, τ_p frequency distributions in Figure 12b show a systematic shift toward higher τ_p as μ_0 decreases. In fact, for very oblique Sun, the frequency of pixels with $\tau_p > 150$ was found to be extremely large. This is shown in Figure 13 for the various cloud models considered. For the inhomogeneous approximation, $\tau_p > 150$ occurs as much as 50% of the time for μ_0 between 0.0 and 0.1 and drops to 0% for μ_0 greater than 0.4. This behavior is also observed when the homogeneous pixel approximation is applied. In this case, approximately 5% of the pixels at very oblique Sun were found to have $\tau_p > 150$.

When the observed reflectance was large, it was interesting to note that the reflectances sometimes ex-

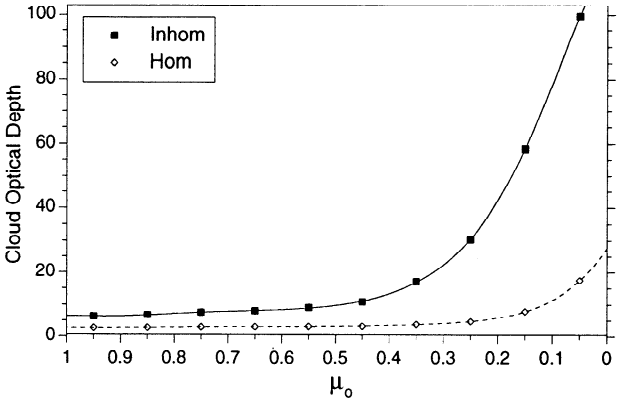

Figure 10. One-year average cloud optical depth versus μ_0 obtained using the inhomogeneous and homogeneous pixel approximations.

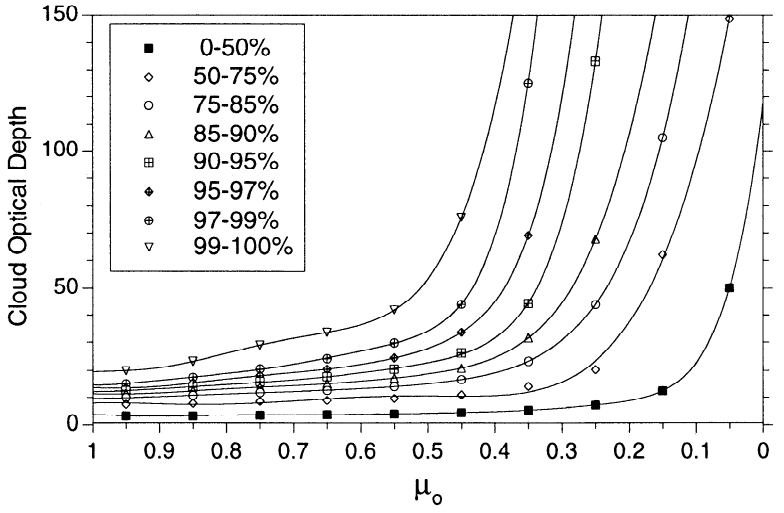

Figure 11a. Cloud optical depth averages for different classes of occurrence for the inhomogeneous pixel approximation. Each line represents an average cloud optical depth for samples lying between the indicated percentile interval.

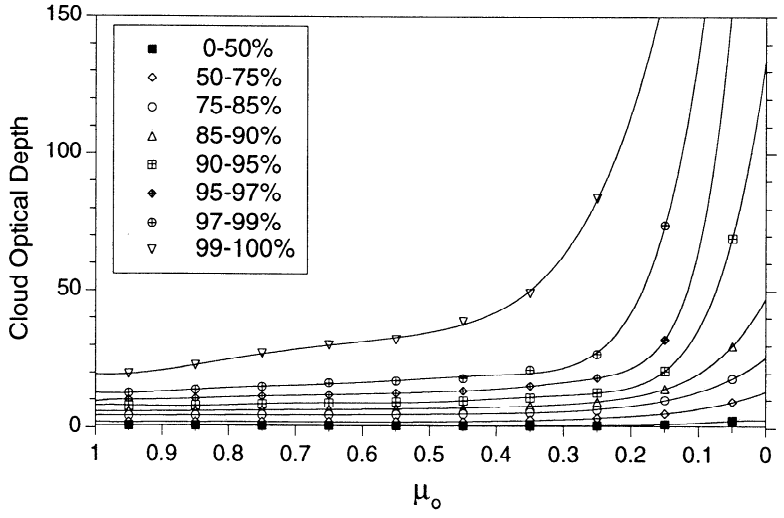

Figure 11b. Cloud optical depth averages for different classes of occurrence for the homogeneous pixel approximation. Each line represents an average cloud optical depth for samples lying between the indicated percentile interval.

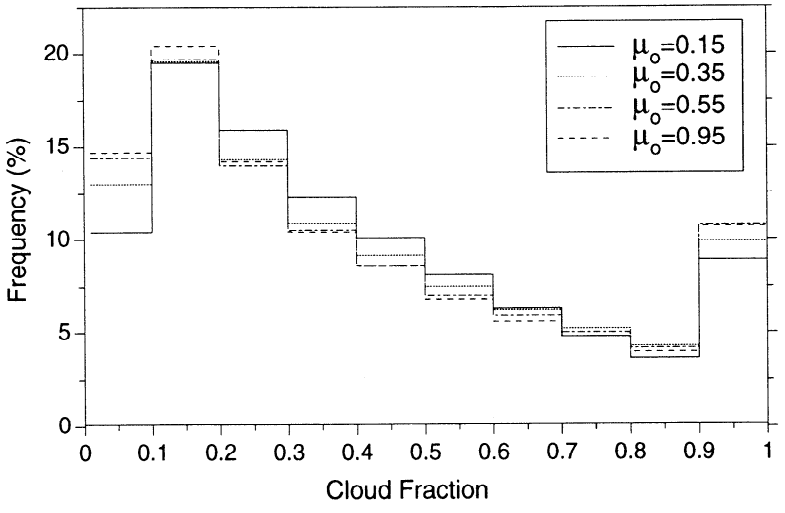

Figure 12a. One-year cloud fraction frequency distributions for various μ_0 obtained using the inhomogeneous pixel approximation.

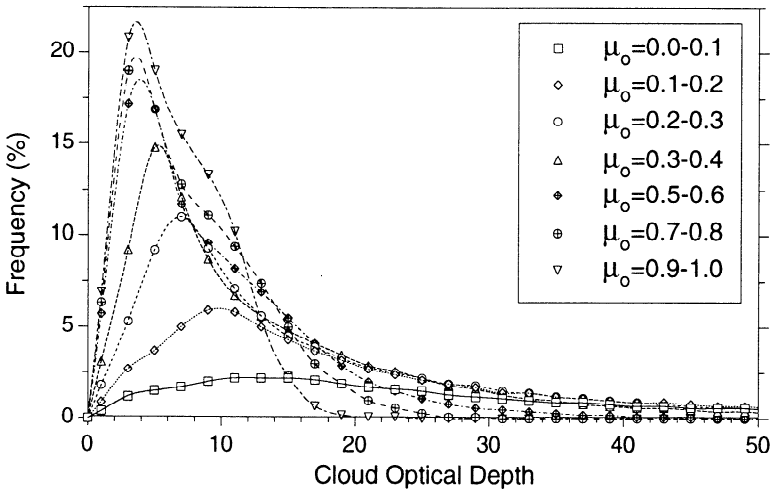

Figure 12b. One-year cloud optical depth frequency distributions for various μ_0 obtained using the inhomogeneous pixel approximation.

ceeded the plane parallel calculations regardless of the cloud fraction or cloud optical depth used in the calculations. As an example, Figure 14 shows a case for a single pixel observation where the reflectance was 54.7%, for $\mu_0 = 0.14$, $\mu = 0.98$ and $\phi = 131°$. When plane parallel calculations were carried out for $f = 1$, cloud optical depths up to 1000, and three different assumptions of clear sky effects, the observed value exceeded the plane parallel value by at least 21% when a cloud top height of 3 km was used, 16% for a cloud top of 6 km, and by 9% when no atmosphere was included above/below the cloud. The occurrence of such cases tended to be restricted to small μ_0 and occurred more frequently as μ_0 decreased.

6. Discussion

The tendency for observed nadir reflectances to exceed plane parallel calculations as the Sun angle becomes more oblique is also apparent in other studies in the literature. Results from an intercomparison between bidirectional reflectance functions from NIMBUS-7 observations and plane parallel calculations by *Stuhlmann et al.* [1985] show that for $\mu_0 < 0.47$, observed bidirectional reflectance functions become increasingly larger than the plane parallel values as μ_0 decreases.

Comparisons between Monte Carlo simulations involving three-dimensional (3D) and plane parallel clouds show similar results. For example, *Kobayashi* [1993] showed that the ratio of the radiance from broken 3D cubical cloud fields to that from plane parallel clouds shows a steady increase at nadir as μ_0 gets smaller. Figure 15 shows sample Monte Carlo calculations (T. Várnai, personal communication, 1995) of 0.5-μm nadir reflectances as a function of μ_0 for a 3D cloud field having an average optical depth of 10 (for a volume extinction coefficient 30 km^{-1}) and a cloud fraction of 0.5.

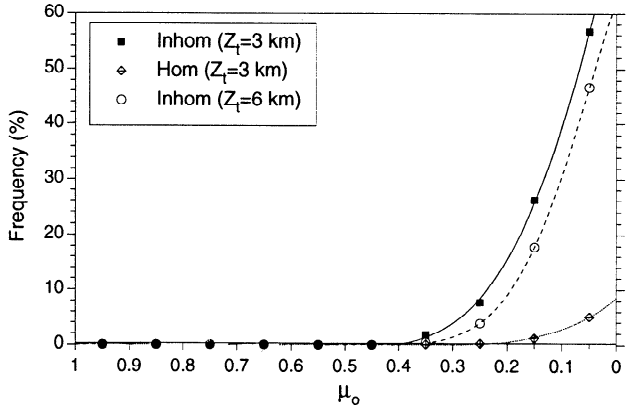

Figure 13. The frequency of pixels with cloud optical depths > 150 for various μ_0 obtained using the inhomogeneous pixel approximation.

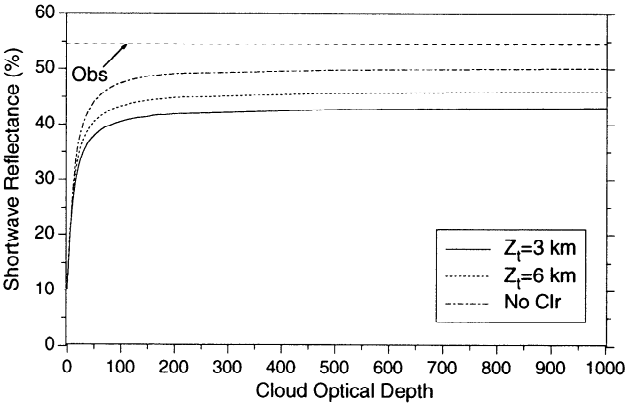

Figure 14. Comparison between shortwave reflectance calculations versus cloud optical depth and an observation at $\mu_0 = 0.14$, $\mu = 0.98$, and $\phi = 131°$ (dashed line). Calculations were performed using a cloud fraction of 1.0 and cloud top heights of 3 and 6 km, as well as for the case when clear sky effects above and below the cloud are not included in the calculation.

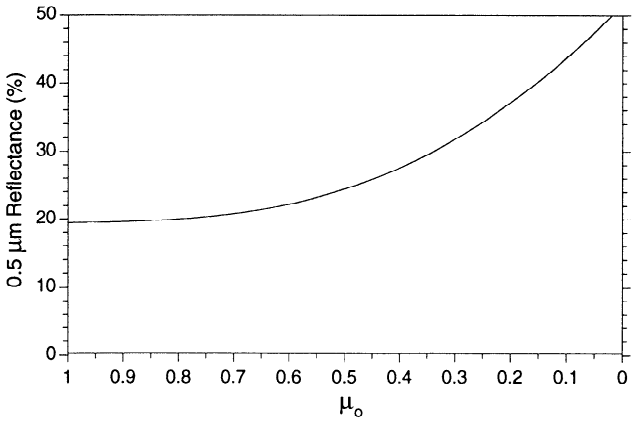

Figure 15. Monte Carlo calculations of 0.5-μm nadir reflectances as a function of μ_0 for a three-dimensional cloud field having an average optical depth of 10 (for a volume extinction coefficient 30 km^{-1}) and a cloud fraction of 0.5 (T. Várnai, personal communication, 1995).

As shown, the reflectance appears to increase with decreasing μ_0 in a manner which is at least qualitatively consistent with the observations.

Thus the inconsistency between the plane parallel calculations and the observations is likely due to the neglect of 3D cloud effects in the plane parallel model approach. While it is beyond the scope of this paper to provide a detailed examination of 3D effects, we note that these may be attributed to various combinations of (1) nonlinear averaging of subpixel inhomogeneity, (2) cloud sides, affecting illuminated and viewed cloud cross sections as well as allowing loss of radiation, (3) cloud top structure, and (4) internal cloud inhomogeneity.

Partial sensitivity to effect (1) is indicated by the difference between the homogeneous and inhomogeneous approximations for subpixel cloud fraction (although the complete effect of nonlinear averaging is likely to be greater than the inhomogeneous approximation made here). Since both approximations show a similar qualitative dependence on μ_0, nonlinear averaging of subpixel inhomogeneity is not the most likely explanation. Neither do we expect the effect of internal cloud inhomogeneity to explain the μ_0 dependence, since this would likely be stronger at high solar elevations where the observed μ_0 dependence is weak. Accordingly, the 3D effects that are most likely to explain the difference between the observed and 1D-modeled μ_0 dependence are the effects of cloud sides and cloud-top structure.

Theoretical studies have shown [*Busygin et al.*, 1973; *McKee and Cox*, 1974; *Aida*, 1977; *Davies*, 1978, 1984; *Bréon*, 1992; *Kobayashi*, 1993] that one contribution which may lead to increased nadir reflectances from 3D clouds involves higher order scattering contributions of radiation which enters the cloud sides and exits through the cloud top. That is, because the cloud sides are exposed to incident radiation, more light is able to enter the cloud and be scattered upward through the top than is possible from a plane parallel cloud. Since the plane parallel discrepancy with μ_0 appears to rise monotonically with cloud optical depth, it is quite likely that the influence of cloud side illumination dominates the observed μ_0 dependence. An additional contribution may be associated with variations in cloud-top structure which can have an important influence on low-order scattering contributions at nadir. As an example, for oblique Sun, sunlit slopes of cloud tops intercept direct solar radiation at smaller angles relative to the surface normal than do flat cloud tops. For a flat cloud top, much of the energy will be concentrated in the forward direction at oblique view angles and a relatively small proportion of scattered radiation will emerge in the nadir direction. Consequently, the relative difference in low-order scattering in the zenith direction from a "bumpy" cloud top compared to a flat top should become progressively larger as μ_0 decreases. Other 3D effects also become more pronounced as the optical depth increases, however, and a deeper analysis is really required to quantitatively distinguish the relative contribution from 3D effects to the observed differences.

In order to assess the overall uncertainty in average reflectance due to the μ_0 bias in cloud optical depth, the average observed reflectances were compared with average calculated reflectances derived using only one set of cloud optical depth and cloud fraction frequency distributions for all μ_0. That is, using the cloud optical depths and cloud fractions derived from observations in the $\mu_0 = 0.9$–1.0 bin, average nadir reflectances were calculated for other values of μ_0 and compared directly with the average observed reflectances in Figure 4. Since the same set of cloud optical depths are used at all μ_0, any differences between the observations and calculations in this comparison will be primarily due to the optical depth bias.

Figure 16 shows the results of this comparison. As expected, large differences between the observed and calculated average reflectances occur as μ_0 decreases.

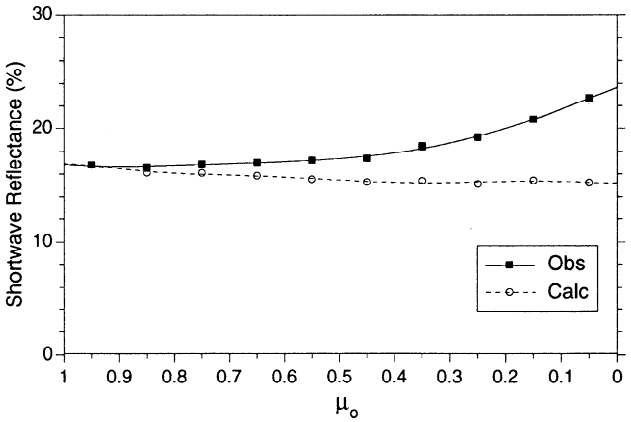

Figure 16. Average reflectance versus μ_0 for the observations and for calculations derived using cloud optical depths and cloud fractions inferred from observations for μ_0 between 0.9 and 1.0.

For $\mu_0 > 0.6$, relative differences in reflectance are less than 10%, on average, and increase to ≈30% at very oblique Sun angles. When these results are further stratified according to pixel brightness, the differences can be even larger. Figure 17 shows average observed and calculated reflectances separately for samples lying above and below the median reflectance (as deduced from the reflectance frequency distributions used to calculate the means in Figure 16). For the darkest 50% of the samples, the plane parallel model appears to provide reasonable estimates of the reflectance at high to moderate solar elevations but is in error by more than 10% for $\mu_0 < 0.45$. For the brightest 50%, however, the discrepancy between observation and plane parallel model reaches ≈10% for $\mu_0 < 0.6$, rising to ≈37% for $\mu_0 = 0.1$. For the brightest 1% of the population, differences as high as 50% were found (not shown here).

Note that the increase in calculated reflectance with decreasing μ_0 for the darkest 50% is due to the larger relative contribution from the clear sky subpixel component. For the darkest scenes, the cloud fractions are generally small and the clouds are thin, so that even though the plane parallel model reflectance of thin clouds decreases slightly with decreasing μ_0, the cloud contribution to the μ_0 dependence in reflectance is not strong enough to reverse the trend of the clear sky contribution.

7. Summary and Conclusions

Shortwave nadir reflectances from plane parallel radiative transfer have been directly compared with 1 year of ERBS scanner measurements for all oceanic scenes between 30°N and 30°S. When matched to observation on a pixel-by-pixel basis (accounting for cloud fraction, curvature effects, and atmospheric effects above and below the cloud), plane parallel theory retrieves cloud optical depths that show a systematic increase with solar zenith angle. In the limit of large solar zenith angle, the retrieved optical depths become extremely large. On average, the largest increases occurred for $\mu_0 \lesssim 0.45$ when subpixel cloud fraction was taken into account. When cloud optical depths were analyzed for different classes of occurrence (deduced by calculating the mean over different percentile intervals), the μ_0 dependence in the cloud optical depth was also found to be sensitive to cloud optical depth. For thin clouds (optical depths $\lesssim 6$), this dependence tended to be strong only at oblique Sun angles. For thicker clouds, the μ_0 dependence was much larger in general and was no longer restricted to small μ_0. In fact, for classes with clouds of optical depth greater than ≈12 at high Sun, this dependence on μ_0 occurred for all solar zenith angles. This was observed for the thickest 10% of the clouds for the inhomogeneous approximation, and the thickest 1% for the homogeneous pixel approximation.

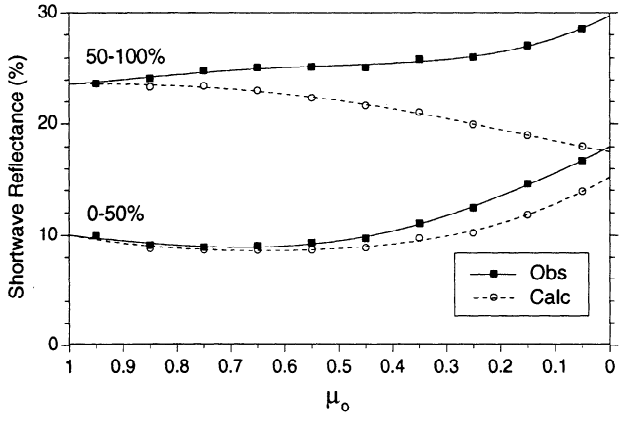

Figure 17. Same as Figure 16 but for reflectances lying below the 50th percentile (0–50%) and for pixels lying between the 50th and 100th percentiles (50–100%).

The absence of strong, systematic, diurnal and latitudinal effects in the observations, together with the high degree of statistical confidence from this very large data set, allows us to conclude that direct use of the plane parallel approach for retrieving cloud optical depth from nadir reflectance is fundamentally flawed for thin clouds at low Sun elevations and for thick clouds in general. That is, because plane parallel nadir reflectances decrease with decreasing μ_0 for a given cloud optical depth, while, on average, observed reflectances show the opposite behavior, plane parallel cloud optical depths inferred from low-resolution satellite measurements suffer from a systematic solar zenith angle dependent bias.

Based on the many studies involving Monte Carlo simulations of 3D cloud fields and on preliminary 3D calculations shown here, it is suggested that the fundamental reason for the differences between the observations and calculations is due to the presence of 3D cloud effects that cannot be accommodated by a plane parallel model. These may include the effects of cloud sides and cloud top structure (e.g., "bumpy" tops), but further analysis is really necessary in order to explain the relative importance of these and other three-dimensional contributions.

The overall (relative) uncertainty in average reflectance due to the μ_0 bias in cloud optical depth was estimated to be less than 10% for $\mu_0 > 0.6$, and as large as 30% at very oblique Sun angles. While the uncertainty in the nadir reflectance was generally small when the reflectance was low, it still exceeded 10% for $\mu_0 < 0.45$ for the thinnest 50% of the clouds, and tended to increase substantially for brighter clouds. For example, relative uncertainties in reflectance for the brightest 50% of the cases could be as high as 37%, while uncertainties as high as 50% were observed for the brightest 1% of the cases.

In closing, we note that these results have obvious implications for remote sensing studies involving the use of plane parallel theory to even small cloud thicknesses at very large solar zenith angles, for example, in high-latitude regions and at sunrise and sunset at all latitudes. Simply correcting for curvature effects and the air mass above the cloud is clearly not sufficient to pro-

duce self-consistent results. The clouds themselves have to be more one-dimensional than is evident from this study, especially by having flatter tops and weaker side effects. The sort of one-dimensional clouds required for the successful application of the plane parallel model do not appear to be statistically important in our data set, which covered oceanic regions from 30°N to 30°S. As a minimum requirement, application of 1D theory to the remote sensing of cloud optical thickness from measurements at nadir should therefore be restricted to thin clouds and small solar zenith angles.

Acknowledgments. This research was supported in part by FCAR (Québec), the Natural Sciences and Engineering Council, the Atmospheric Environment Service (Canada), and the Jet Propulsion Laboratory under contract 959085. We would like to thank Tamás Várnai for making his Monte Carlo results available.

References

Aida, M.A., Scattering of solar radiation as a function of cloud dimension and orientation, *J. Quant. Spectrosc. Radiat. Transfer*, *17*, 303–310, 1977.

Barkstrom, B.R., E. Harrison, G. Smith, R. Green, J. Kibler, R. Cess, and the ERBE Science Team, Earth Radiation Budget Experiment (ERBE) archival and April 1985 results, *Bull. Am. Meteorol. Soc.*, *70*, 1254–1262, 1989.

Bohren, C.F., and D.R. Huffman, *Absorption and Scattering of Light by Small Particles*, 530 pp., John Wiley, New York, 1983.

Bréon, F.-M., Reflectance of broken cloud fields: Simulation and parameterization, *J. Atmos. Sci.*, *49*, 1221–1232, 1992.

Busygin, V.P., N.A. Yevstratov, and Y.M. Feigel'son, Optical properties of cumulus clouds, and radiant fluxes for cumulus cloud cover, *Izv. Acad. Sci. USSR*, Engl. Transl., *9*, 1142–1151, 1973.

Coakley, J.A., Reflectivities of uniform and broken layered clouds, *Tellus*, *43B*, 420–433, 1991.

Coakley, J.A. Jr., and R. Davies, The effect of cloud sides on reflected solar radiation as deduced from satellite observations, *J. Atmos. Sci.*, *43*, 1025–1035, 1986.

Davies, R., The effect of finite geometry on the three-dimensional transfer of solar irradiance in clouds, *J. Atmos. Sci.*, *35*, 1712–1725, 1978.

Davies, R., Reflected solar radiances from broken cloud scenes and the interpretation of scanner measurements, *J. Geophys. Res.*, *89*, 1259–1266, 1984.

Davies, R., Spatial autocorrelation of radiation measured by the Earth Radiation Budget Experiment: Scene inhomogeneity and reciprocity violation, *J. Geophys. Res.*, *99*, 20,879–20,887, 1994.

Davies, R., W.L. Ridgway, and K.-E. Kim, Spectral absorption of solar radiation in cloudy atmospheres: A 20 cm^{-1} model, *J. Atmos. Sci.*, *41*, 2126–2137, 1984.

Deirmendjian, D., *Electromagnetic Scattering on Spherical Polydispersions*, 290 pp., Elsevier, New York, 1969.

Durkee, P.A., F. Pfeil, E. Frost, and R. Shema, Global analysis of aerosol particle characteristics, *Atmos. Environ.*, *25A*, 2457–2471, 1991.

Hale, G.M., and M.R. Querry, Optical constants of water in the 200-nm to 200 μm wavelength region, *Appl. Opt.*, *12*, 555–563, 1973.

Hartmann, D.L., and E.E. Recker, Diurnal variation of outgoing longwave radiation in the tropics, *J. Clim. Appl. Meteorol.*, *25*, 800–812, 1986.

Hoppel, W.A., J.W. Fitzgerald, G.M. Frick, R.E. Larson, and E.J. Mack, Aerosol size distributions and optical properties found in the marine boundary layer over the Atlantic Ocean, *J. Geophys. Res.*, *95*, 3659–3686, 1990.

Kneizys, F.X., E.P. Shettle, L.W. Abreu, J.H. Chetwynd Jr., G.P. Anderson, W.O. Gallery, J.E.A. Selby, and S.A. Clough, Users Guide to LOWTRAN 7, Rep. *AFGL-TR-88-0177*, 137 pp., Air Force Geophys. Lab., Hanscom AFB, Mass., 1988.

Kobayashi, T., Effects due to cloud geometry on biases in the albedo derived from radiance measurements, *J. Clim.*, *6*, 120–128, 1993.

Koepke, P., and H. Quenzel, Turbidity of the atmosphere determined from satellite: Calculation of optimum viewing geometry, *J. Geophys. Res.*, *84*, 7847–7856, 1979.

Kopia, L.P., The Earth Radiation Budget Experiment scanner instrument, *Rev. Geophys.*, *24*, 400–406, 1986.

Machado, L.A.T., M. Desbois, and J.-P. Duval, Structural characteristics of deep convective systems over tropical Africa and Atlantic Ocean, *Mon. Weather Rev.*, *120*, 392–406, 1992.

McKee, T.B., and S.K. Cox, Scattering of visible radiation by finite clouds, *J. Atmos. Sci.*, *31*, 1885–1892, 1974.

Minnis, P., Viewing zenith angle dependence of cloudiness determined from coincident GOES East and GOES West data, *J. Geophys. Res.*, *94*, 2303–2320, 1989.

Minnis, P., and E.F. Harrison, Diurnal variability of regional cloud and clear-sky radiative parameters derived from GOES data, II, November 1978 cloud distributions, *J. Clim. Appl. Meteorol.*, *23*, 1012–1031, 1984.

Prospero, J.M., R.J. Charlson, V. Mohnen, R. Jaenicke, A.C. Delany, J. Moyers, W. Zoller, and K. Rahn, The atmospheric aerosol system: An overview, *Rev. Geophys. Space Phys.*, *21*, 1607–1629, 1983.

Rossow, W.B., and R.A. Schiffer, ISCCP cloud products, *Bull. Am. Meteorol. Soc.*, *72*, 2–20, 1991.

Stamnes, K., S.-C. Tsay, W. Wiscombe, and K. Jayaweera, Numerically stable algorithm for discrete-ordinate-method radiative transfer in multiple scattering and emitting layered media, *Appl. Opt.*, *24*, 2502–2509, 1988.

Stuhlmann, R., P. Minnis, and G.L. Smith, Cloud bidirectional reflectance functions: A comparison of experimental and theoretical results, *Appl. Opt.*, *24*, 396–401, 1985.

Toon, O.B., and J.B. Pollack, A global average model of atmospheric aerosols for radiative transfer calculations, *J. Appl. Meteorol.*, *15*, 225–246, 1976.

Warren, S.G., C.J. Hahn, J. London, R.M. Chervin, and R.L. Jenne, Global distribution of total cloud cover and cloud type amounts over the ocean, *NCAR Tech. Note, TN-317+STR*, 42 pp. + 170 maps, 1988.

Wielicki, B.A., and R.N. Green, Cloud identification for ERBE radiative flux retrieval, *J. Appl. Meteorol.*, *28*, 1133-1146, 1989.

Wielicki, B.A., and L. Parker, On the determination of cloud cover from satellite sensors: The effect of sensor spatial resolution, *J. Geophys. Res.*, *97*, 12,799–12,823, 1992.

R. Davies, Institute of Atmospheric Physics, PAS Bldg. 81, University of Arizona, Tucson, AZ 85721. (e-mail: davies @air.atmo.arizona.edu)

N. G. Loeb, Department of Atmospheric and Oceanic Sciences, McGill University, 805 Sherbrooke St. W., Montreal, Québec, H3A 2K6, Canada.

(Received May 15, 1995; revised October 17, 1995; accepted October 17, 1995.)